

## Article

# Influence of the Experimental Setup on Electromagnetic Pulses in the VHF Band at Relativistic High-Power Laser Facilities

Michael Ehret <sup>1,\*</sup>, Luca Volpe <sup>1,2</sup>, Jon Imanol Apiñaniz <sup>1</sup>, Maria Dolores Rodríguez-Frías <sup>1,3</sup>  
and Giancarlo Gatti <sup>1</sup>

<sup>1</sup> Centro de Laseres Pulsados (CLPU), 37185 Villamayor, Spain

<sup>2</sup> Física Aplicada a las Ingenierías Aeronáutica, Universidad Politécnica de Madrid, 28040 Madrid, Spain

<sup>3</sup> Física y Matemáticas, Universidad de Alcalá, 28801 Madrid, Spain

\* Correspondence: mehret@clpu.es; Tel.: +34-923-338-121

**Abstract:** We present experimental results for the controlled mitigation of the electromagnetic pulses (EMPs) produced in the interactions of a 1 PW high-power 30 fs Ti:Sa laser VEGA-3 with solid-density targets transparent to laser-forward-accelerated relativistic electrons. This study aims at the band of very high frequencies (VHFs), i.e., those in the hundreds of MHz, which comprise the fundamental cavity modes of the rectangular VEGA-3 vacuum chamber. We demonstrate mode suppression by a tailoring of the laser-produced space charge distribution.

**Keywords:** laser-generated EMPs; EMP mitigation; high-power laser; relativistic laser–plasma

## 1. Introduction

Advances in laser technology have led to the emergence of high-power Ti:Sa laser systems [1–9] that are able to deliver laser pulses up to several PW at a high-repetition rate of 0.05 Hz to 1 Hz. In principle, these systems allow for the generation of secondary sources that exist in a wide range, from ionizing radiation [10–13] to XUV- and THz-pulses [14–17], as well as current pulses [18] when they are focused to relativistic intensities. Recent developments toward high-repetition-rate ion sources [19,20] have aimed at the generation of pulsed, bright ion beams by well-known mechanisms such as Target Normal Sheath Acceleration (TNSA) [21,22], Radiation Pressure Acceleration [23], etc. [11], which are beneficial to isotope production [24,25], positron emission tomography [26], ion beam microscopy [27], particle-induced X-ray emission [28], as well as inertial confinement fusion [29]. The mechanisms rely on the build up of large accelerating potentials, which are the consequence of electron dynamics that are also the source of ultra-strong electromagnetic pulses (EMPs) [30].

When a focused laser pulse interacts with a  $\mu\text{m}$ -scale solid foil target at ultra-high intensities in the range of  $1 \times 10^{18} \text{ W cm}^{-2}$  to  $1 \times 10^{20} \text{ W cm}^{-2}$ , the extraction of electrons ensues from Brunel-type resonance absorption [31,32] and ponderomotive  $j \times B$  acceleration [33,34]. The electron dynamics give rise to the generation of intense EMPs with broad bandwidths, ranging from radio frequencies [35] to X-rays [36]. As they are particularly important for very high frequency (VHF) bands, the targets of the frequencies attain a strong positive net-charge due to laser-accelerated electrons that are able to escape the rising potential barrier [37]. These electrons predominantly propagate in a laser-forward direction [38], and they yield an asymmetric charge separation. They distribute a negative charge across the experimental setup when they stop on the ns-timescale of their time of flight. Return currents rise on the same timescale of ns [39], and resonances within the cavity of the experimental vacuum chamber can build up. The resulting broadband EMPs bear the geometry of the experimental setup in their mode structure [30,40].

The semiconductor electronics widely used in metrology devices or diagnostics are susceptible to EMPs in the VHF and ultra-high frequency bands [41]. The mitigation



**Citation:** Ehret, M.; Volpe, L.; Apiñaniz, J.I.; Rodríguez-Frías, M.D.; Gatti, G. Influence of the Experimental Setup on Electromagnetic Pulses in the VHF Band at Relativistic High-Power Laser Facilities. *Photonics* **2024**, *11*, 459. <https://doi.org/10.3390/photonics11050459>

Received: 18 March 2024

Revised: 10 May 2024

Accepted: 12 May 2024

Published: 14 May 2024



**Copyright:** © 2024 by the authors. Licensee MDPI, Basel, Switzerland. This article is an open access article distributed under the terms and conditions of the Creative Commons Attribution (CC BY) license (<https://creativecommons.org/licenses/by/4.0/>).

of EMPs is especially important in light of future applications that will require complex electronics systems for control and quality management. This work (i) proposes new means for measuring EMPs in the VHF band by deploying commercial broadband antennas, and it also (ii) demonstrates the efficient tailoring of electromagnetic modes by geometrical changes to the experimental setup.

## 2. Materials and Methods

For this work, EMPs were generated by the interaction of the PW-class VEGA-3 laser at Centro de Láseres Pulsados (CLPU, Villamayor, Spain) [42] with a double chirp pulse amplification Ti:Sa system that had a central wavelength of 800(10) nm.

### 2.1. Laser- and Target-System

A cross-polarized wave system was used to enhance the coherent contrast and reduce the throughput of the amplified spontaneous emission. The laser pulse was focused to relativistic intensities onto a 3.0(3)  $\mu\text{m}$ -thin, solid-density aluminum target. The target system holds 120 fresh surfaces for laser interaction in a matrix framed by aluminum plates that have recesses of a 1 mm diameter for each interaction zone, and these are exchanged by a 3D motorized mount [42]. The target system is vertically inclined by 12.5(5) $^\circ$  with respect to the laser axis to avoid back-reflection into the beamline. Before interaction, the laser pulse is amplified to a pulse energy  $E_L$  up to 25 J per pulse, which is then compressed down to a 30 fs duration with a grating compressor and focused via a  $f/10$  off-axis parabola to a focal spot size of a 12  $\mu\text{m}$  Full-Width-at-Half-Maximum (FWHM). Both, the target positioning and the spatial characterization of the laser focal spot were conducted using a parallel imaging system. A motorized microscope objective picked up the laser pulse on-axis to the focal spot, and an achromatic doublet imaged the far-field of the beam onto a CCD camera. It was ensured that the numerical aperture of the imaging system was large enough to capture the laser pulse. The first Airy-disk enclosed 6.9 J, which was extrapolated from low-energy focus measurements, such as the laser intensity that reaching  $1.3 \times 10^{20} \text{ W cm}^{-2}$  on target. The normalized vector potential of the laser pulse calculated was as  $a_0 \approx 7.8$ .

### 2.2. Space Charge Dynamics

The average energy  $k_B T_h$  that was transferred to an electron of the relativistic population approximately followed [43] with the ponderomotive scaling [22] of

$$k_B T_h = m_e c^2 (\sqrt{1 + a_0^2} - 1) = 3.5 \text{ MeV}, \quad (1)$$

where  $m_e$  is the electron rest mass and  $c$  denotes the speed of light in a vacuum.

As the VEGA laser pulse showed no pre-pulses that were capable of inducing a density modulation across all of the 3  $\mu\text{m}$ -thick target [42], the main acceleration mechanism of the charged particles was TNSA. In TNSA, the population of laser-heated relativistic electrons escape the target, and the successive potential dynamics lead to the formation of sheath fields that are capable of accelerating ionized surface contaminants up to several tens of  $\text{MeV u}^{-1}$  [44]. The ions co-propagate with slow electrons and form a quasi-neutral beam, which we will neglect in the following. The building up of a positive potential in the target through escaping relativistic electrons induces a return current toward the target. Note that the target's only connection to the ground is via the motor block and the chamber itself. The deposition of electrons and return of the current lead to wall currents in the chamber, which, in turn, allow for resonant cavity modes to grow. With a focus on the MHz domain, the charging of the target on the ps timescale [37] is instantaneous: the target is initially at a net positive potential and electrons charge distributions are instantly deposited across the environment of the target.

### 2.3. Experimental Environment

The experimental setup is shown in Figure 1. The experimental environment was kept in a high-vacuum of  $1 \times 10^{-6}$  mbar, which allowed for (i) focusing the laser pulse to high intensities above the typical ionization threshold of matter at  $1 \times 10^8 \text{ W cm}^{-2}$  to  $1 \times 10^{12} \text{ W cm}^{-2}$  [45] and (ii) compressing the laser pulse beforehand without damage to the grating compressor of the VEGA-3 laser system. The interaction point was 31 cm off-center (i.e., toward the focusing parabola) with respect to the vacuum chamber. The vacuum chamber was made of aluminum, comprising dielectric view ports, and it was grounded via a spike earthing electrode.

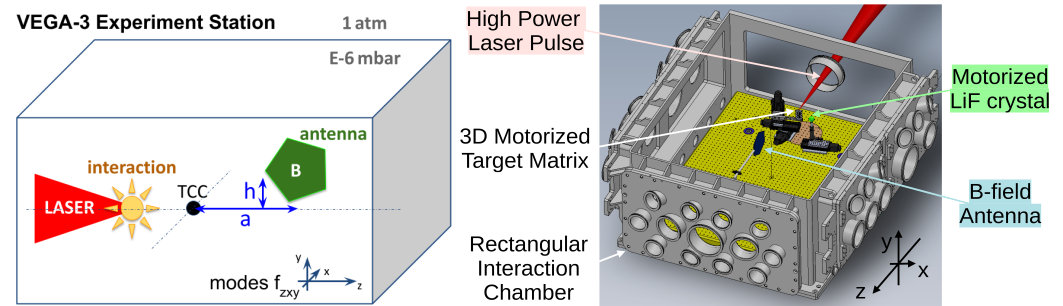


**Figure 1.** Experimental setup sketch (left) and computer-aided drawing (right) of the pulsed laser interaction with a solid-density target located off-center with respect to the rectangular vacuum vessel, which served as the interaction chamber. The EMPs were detected with a B-field antenna located behind the interaction region (in a laser forward direction) and above the path of the horizontal plane. A LiF crystal was located on a motorized stage to be moved in and out of the path of the laser-accelerated charged particles from the target rear side.

### 2.4. Cavity Modes

The inclination of the target leads to a deposition of negative charge in a wide opening angle ranging from one corner of the interaction chamber to the laser forward direction, see figure (Figure 2A). The relativistic electron beam is completely stopped in the cm thick wall of the vacuum chamber. Transverse and longitudinal electric fields are likely to build up. Return currents in the skin depth of the chamber walls then stream longitudinally and radially, causing a transverse azimuthal and radially toroidal magnetic field. The excited modes are expected to be  $f_{100}$ ,  $f_{001}$ , and higher orders. The positive potential of the target and radial return currents can excite modes such as  $f_{101}$ ,  $f_{010}$ ,  $f_{110}$ ,  $f_{111}$ , as well as higher orders.

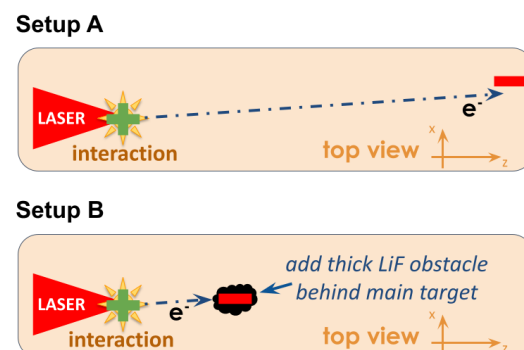


**Figure 2.** A first setup (A) that comprises only the aluminum target and allows for a free propagation of accelerated species until they reach the chamber wall. The setup change (B) introduces an obstacle on the path of relativistic electrons, which are intended to change the seed space charge distribution and thus the build up of cavity modes.

In a medium with the speed of light  $c$ , resonant modes have the following frequencies:

$$f_{mnp} = \frac{c}{2} \cdot \sqrt{\left(\frac{m}{\Delta x}\right)^2 + \left(\frac{n}{\Delta y}\right)^2 + \left(\frac{p}{\Delta z}\right)^2} . \quad (2)$$

The mode numbers  $\{m, n, p\}$  correspond to dimensions  $\{\Delta x, \Delta y, \Delta z\}$  for the width, height, and length of the vacuum vessel, respectively. The width in a laser-transverse direction is  $\Delta x \in [120 \text{ cm}; 169 \text{ cm}]$ , the height is  $\Delta y \in [60 \text{ cm}; 70 \text{ cm}]$ , and the length in a laser-forward direction is  $\Delta z \in [164 \text{ cm}; 175 \text{ cm}]$ . Here, the lower bound is given by the rectangular inner surface. The outer bound is given by ports, flanges, and window surfaces, which are not expected to play a major role for resonances but will contribute to losses. The relevant cavity modes are

$f_{001} = 91 \text{ MHz},$	$f_{111} = 294 \text{ MHz},$
$f_{100} = 125 \text{ MHz},$	$f_{202} = 310 \text{ MHz},$
$f_{101} = 155 \text{ MHz},$	$f_{112} = 334 \text{ MHz},$
$f_{002} = 183 \text{ MHz},$	$f_{211} = 365 \text{ MHz},$
$f_{010} = 250 \text{ MHz},$	$f_{004} = 366 \text{ MHz},$
$f_{200} = 250 \text{ MHz},$	$f_{203} = 371 \text{ MHz},$
$f_{011} = 266 \text{ MHz},$	$f_{300} = 375 \text{ MHz},$
$f_{003} = 274 \text{ MHz},$	$f_{212} = 398 \text{ MHz},$
$f_{110} = 279 \text{ MHz}.$	

### 2.5. EMP Detection

The primary EMP diagnostic used in this study was a commercial passive, calibrated B-field antenna with large bandwidth that ranged from 9 kHz to 400 MHz (Aaronia MDF9400). The outgassing of the antenna was tested before use, see Figure 3. The magnetic field antenna was positioned inside the vacuum chamber in the vertical plane of the laser propagation, which had a longitudinal value of  $a = 17.5 \text{ cm}$  behind the center of the cavity and  $h = 17.5 \text{ cm}$  above the horizontal center plane. The signal was transported via calibrated double-shielded SMA cables and was sent through a floating feed through. The conductive connection of the SMA cables and chamber was avoided completely, and the grounding was achieved via the wall plug of the data recorder. The waveforms were captured with an oscilloscope of a 1 GHz bandwidth and 2.5 GS/s sampling rate. The results displayed in this work were corrected for attenuation and the bandwidth limitations of the full measurement circuit, which was achieved by taking into account the transfer function of the circuit. In the frequency domain, the division of the oscilloscope measurement by the transfer function of the coaxial line between the antenna and analog digital converter will lead to an input signal by the antenna. The latter we call the corrected signal for clarity.

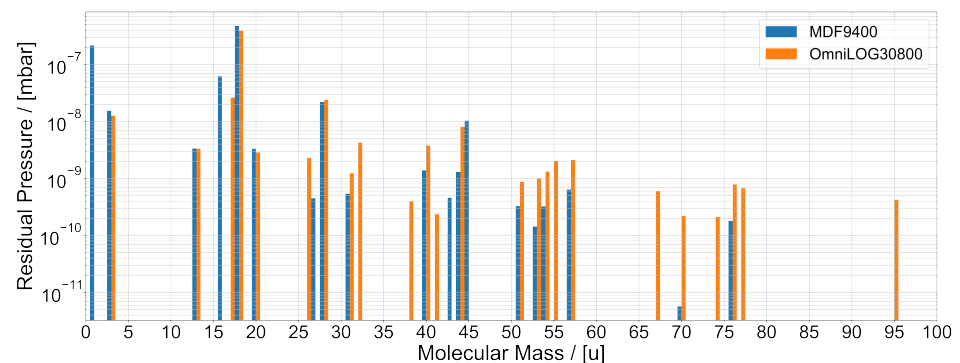


**Figure 3.** The residual pressure of the detected molecules in a high vacuum chamber for commercially available EMP antennas from Aaronia.

### 3. Results

In order to unravel the changes to the mode structure in the VHF band, the standard mode structure in the vacuum chamber was first characterized, which was then followed by an obstacle being introduced to the path of the ejected electrons in order to modify the seed space charge distribution.

#### 3.1. Standard Mode Structure in the VHF Band

The time-integrated Fast Fourier Transform of the resulting time-resolved waveform data acquired during the experiment is shown in Figure 4. We defined the signal (blue points) as the measurement by the oscilloscope, and the corrected signal (green points) as the input signal from the antenna, which was calculated from the measurement. The latter was achieved by the division of the measurement by the transfer function of the coaxial line between the antenna and analog digital converter of the oscilloscope in the frequency domain. One notes the strong mode  $f_{101}$ , which was selected by the initial diagonal space charge fields. The respective fundamentals  $f_{100}$  and  $f_{001}$  were clearly visible. In addition to the cavity modes, the cylindrical metallic 1/2-inch mounts of the optics with a length ranging from 20 cm to 30 cm produced spectral peaks with antenna fields in a range from 250 MHz to 372 MHz. Their resonance frequencies were defined by a match of multiples of  $\lambda/4$  with the length of the grounded monopole rod. Above these frequencies, there was a clear peak at 385(10) MHz. This corresponded to 19(1) cm, and might be related to the motorized translation stage holding the target.

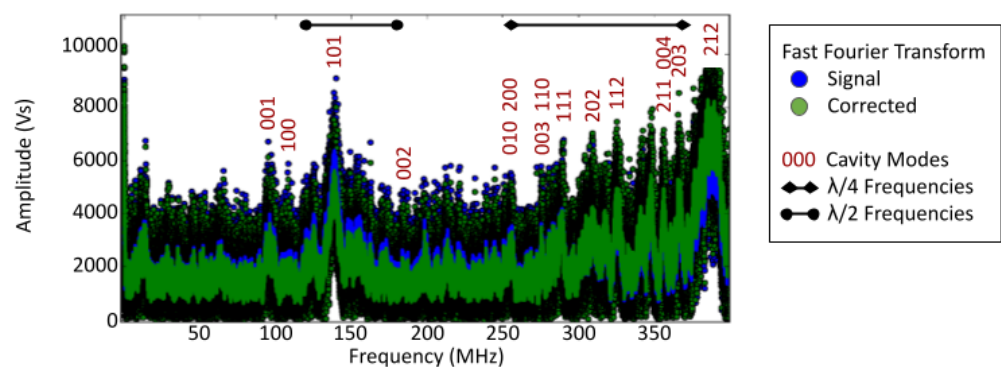


**Figure 4.** The time-integrated spectrum of the magnetic field derived from the oscilloscope recordings of B-field antenna measurements in the VEGA-3 interaction chamber for shots on solid targets, with an indication of identified rectangular cavity modes and the resonance of the vertical stalks that hold optics ( $\lambda/4$ ). Note that the signal denotes the measurement by the oscilloscope, and the corrected signal denotes the input signal from the antenna, which was calculated from the measurement.

#### 3.2. Modified Mode Structure in the VHF Band

In order to alter the mode structure, a beam dumper from inorganic lithium fluoride (LiF) with a thickness of  $\approx 1.5$  cm and a diameter of  $\approx 2.5$  cm was positioned at 1 cm behind the aluminum target, see Figure 2B. The LiF and the axis were defined by the target normal and target center as being colinear. The crystal acted as an electron catcher, thereby removing part of the forward-propagating space charge. Due to a close positioning of the LiF catcher with respect to the target, practically the full solid angle in the laser-forward direction was covered. The arrangement was chosen to weaken the fundamental modes in the transverse and longitudinal directions. The stopping of electrons was simulated with the Monte Carlo simulation code CASINO [46] for a LiF crystal of a density of  $1.06756 \text{ g cm}^{-3}$ . It stops all electrons up to an energy of 2.8 MeV, which presumably represent a significant part of the electron population.

The mode structure with the LiF crystal installed is shown in Figure 5. We defined the signal (blue points) as the measurement by the oscilloscope, and the corrected signal (green points) as the input signal from the antenna, which was calculated from the mea-

surement. The latter was achieved by division of the measurement by the transfer function of the coaxial line between the antenna and analog digital converter of the oscilloscope in the frequency domain. One notes a reduction in the fundamental mode in the longitudinal direction, a removal of the fundamental mode in the transverse direction, and a clear reduction in energy in mode  $f_{101}$ . The return current in the mount of the beam dumper, which was about 20.5 cm in height, manifested in a spectral peak that appeared at 366(4) MHz—on the left edge of the large peak, which might be attributed to the motorized translation stage that was discussed above.

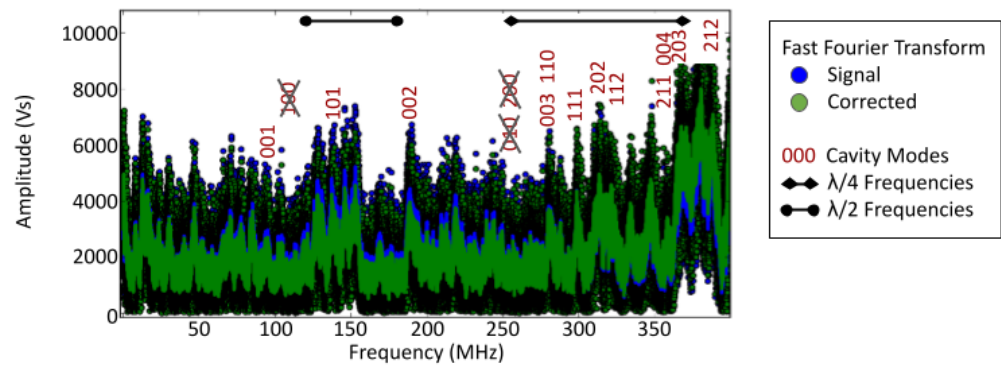


**Figure 5.** The time-integrated spectrum of the magnetic field derived from the oscilloscope recordings of B-field antenna measurements in the VEGA-3 interaction chamber for shots on solid targets with an inserted LiF beam dump shortly behind the solid target, with an indication of the identified rectangular cavity modes and the resonance of the vertical stalks that hold optics ( $\lambda/4$ ). Note that the signal denotes the measurement by the oscilloscope, and the corrected signal denotes the input signal from the antenna, which was calculated from the measurement.

#### 4. Discussion

The results prove that a tailored geometrical modification of the experimental environment allows one to influence the VHF mode structure in the cavity. The build up of modes follows the geometry of the initial space charge distribution, which is the seed for cavity modes. The selection of suppressed modes is implicit; therefore, the method is only suitable if important geometrical modifications do not perturb the experiment, or if the presence of a huge obstacle is favorable.

In this work, a LiF crystal was used as a catcher in accordance with experiments that aim at a conversion of laser-accelerated ions to neutrons [47–49]. This scheme for EMP tailoring was not limited to the use of LiF as a catcher material, but it also has validity in other pitcher–catcher schemes [50]. The effectiveness of thick secondary catcher targets with respect to EMP tailoring aligns well with experimental requirements in many pitcher–catcher experiments, where thicker catcher targets represent good converters for the increased stopping of ion beam incidents.

#### 5. Conclusions

Excited cavity modes were clearly detected by a compact EMP detection system based on a cheap commercial broadband range of 9 kHz to 400 MHz magnetic field antennas of a 15 cm diameter. The results show the respective fundamental modes  $f_{100}$  of 125 MHz and  $f_{001}$  of 91 MHz, as well as the antenna fields issued by cylindrical metallic 1/2-inch mounts in a range of 250 MHz to 372 MHz. Above these frequencies, there was a clear peak at 385(10) MHz, which might be related to the motorized translation stage holding the target.

This work shows that the EMP mode structure inside the vacuum cavity can be tailored by a modification of the experimental geometry. The introduction of a beam block to the propagation path of relativistic electrons suppresses the longitudinal mode  $f_{100}$  and clearly reduces the  $f_{101}$  mode. VHF EMPs are relevant in science and technology in many fields, ranging from homeland security [51] to medicine [52], due to their potential hazards and

promising applications. Their controlled mitigation and generation will pave the ground for further studies in those fields.

**Author Contributions:** Conceptualization, M.E.; methodology, M.E.; software, M.E.; validation, M.E. and G.G.; formal analysis, M.E.; investigation, M.E. and J.I.A.; resources, M.D.R.-F., L.V. and G.G.; data curation, M.E.; writing—original draft preparation, M.E. and J.I.A.; writing—review and editing, M.E.; visualization, M.E.; supervision, M.E.; project administration, G.G.; funding acquisition, L.V. and G.G. All authors have read and agreed to the published version of the manuscript.

**Funding:** This research was funded by the European Union’s Horizon 2020 research and innovation program under grant agreement no. 871161.

**Institutional Review Board Statement:** Not applicable.

**Informed Consent Statement:** Not applicable.

**Data Availability Statement:** Data will be made available if a reasonable request is addressed to the authors.

**Acknowledgments:** This work was supported by the European IMPULSE project with funding from the European Union’s Horizon 2020 research and innovation program under grant agreement no. 871161. The authors are grateful to Pilar Puyuelo-Valdes for organizing the underlying experiment as the responsible link scientist from the facility, as well as José Manuel Álvarez (CLPU) as the principal investigator for allowing us to conduct this parasitic study during his experimental campaign. We thank Pablo Vicente for his help with the computer-aided drawings. This work would not have been possible without the help of the laser and engineering teams at CLPU. Special thanks are given for the greatly appreciated support provided by the workshops of CLPU. We thank for the technical support by Juan Hernández for the vacuum measurements.

**Conflicts of Interest:** The authors declare no conflicts of interest.

## References

1. Jeong, T.M.; Lee, J. Femtosecond petawatt laser. *Ann. Phys.* **2014**, *526*, 157. [[CrossRef](#)]
2. Hooker, C.J.; Blake, S.; Chekhlov, O.; Clarke, R.J.; Collier, J.L.; Divall, E.J.; Ertel, K.; Foster, P.S.; Hawkes, S.J.; Holligan, P.; et al. Commissioning the Astra Gemini Petawatt Ti:Sapphire Laser System. In Proceedings of the Conference on Lasers and Electro-Optics/Quantum Electronics and Laser Science Conference and Photonic Applications Systems Technologies, San Jose, CA, USA, 4–9 May 2008; CLEO (OSA Technical Digest), paper JThB2 (2008).
3. Yu, T.J.; Lee, S.K.; Sung, J.H.; Yoon, J.W.; Jeong, T.M.; Lee, J. Generation of high-contrast, 30 fs, 1.5 PW laser pulses from chirped-pulse amplification Ti:sapphire laser. *Opt. Express* **2012**, *20*, 10807. [[CrossRef](#)]
4. Leemans, W.P.; Daniels, J.; Deshmukh, A.; Gonsalves, A.J.; Magana, A.; Mao, H.S.; Mittelberger, D.E.; Nakamura, K.; Riley, J.R.; Syversrud, D. Bella laser and operations. In Proceedings of the PAC 2013, Pasadena, CA, USA, 29 September–4 October 2013; pp. 1097–1100.
5. Sung, J.H.; Lee, H.W.; Yoo, J.Y.; Yoon, J.W.; Lee, C.W.; Yang, J.M.; Son, Y.J.; Jang, Y.H.; Lee, S.K.; Nam, C.H. 4.2 PW, 20 fs Ti: Sapphire laser at 0.1 Hz. *Opt. Lett.* **2017**, *42*, 2058. [[CrossRef](#)] [[PubMed](#)]
6. Li, W.; Gan, Z.; Yu, L.; Wang, C.; Liu, Y.; Guo, Z.; Xu, L.; Xu, M.; Hang, Y.; Xu, J.; et al. 339 J high-energy Ti: Sapphire chirped-pulse amplifier for 10 PW laser facility. *Opt. Lett.* **2018**, *43*, 5681. [[CrossRef](#)]
7. Lureau, F.; Matras, G.; Chalus, O.; Derycke, C.; Morbieu, T.; Radier, C.; Casagrande, O.; Laux, S.; Ricaud, S.; Rey, G.; et al. High-energy hybrid femtosecond laser system demonstrating  $2 \times 10$  PW capability. *High Power Laser Sci. Eng.* **2020**, *8*, e43. [[CrossRef](#)]
8. Danson, C.; Hillier, D.; Hopps, N.; Neely, D. Petawatt class lasers worldwide. *High Power Laser Sci. Eng.* **2015**, *3*, e3. [[CrossRef](#)]
9. Wang, Y.; Wang, S.; Rockwood, A.; Luther, B.M.; Hollinger, R.; Curtis, A.; Calvi, C.; Menoni, C.S.; Rocca, J.J. 0.85 PW laser operation at 3.3 Hz and high-contrast ultrahigh-intensity  $\lambda = 400$  nm second-harmonic beamline. *Opt. Lett.* **2017**, *42*, 3828–3831. [[CrossRef](#)] [[PubMed](#)]
10. Daido, H.; Nishiuchi, M.; Pirozhkov, A.S. Review of laser-driven ion sources and their applications. *Rep. Prog. Phys.* **2012**, *75*, 056401. [[CrossRef](#)] [[PubMed](#)]
11. Borghesi, M. Ion Acceleration: TNSA and Beyond. In *Springer Proceedings in Physics*; Springer: Berlin/Heidelberg, Germany, 2019; Volume 231.
12. Tajima, T.; Malka, V. Laser plasma accelerators. *Plasma Phys. Control. Fusion* **2012**, *62*, 034004. [[CrossRef](#)]
13. Norreys, P.A.; Santala, M.; Clark, E.; Zepf, M.; Watts, I.; Beg, F.N.; Krushelnick, K.; Tatarakis, M.; Dangor, A.E.; Fang, X.; et al. Observation of a highly directional  $\lambda$ -ray beam from ultrashort, ultraintense laser pulse interactions with solids. *Phys. Plasmas* **1999**, *6*, 2150–2156. [[CrossRef](#)]

14. Lichters, R.; Meyer-ter-Vehn, J.; Pukhov, A. Short-pulse laser harmonics from oscillating plasma surfaces driven at relativistic intensity. *Plasmas* **1996**, *3*, 3425. [[CrossRef](#)]
15. Corkum, P.B.; Krausz, F. Attosecond science. *Nat. Phys.* **2007**, *3*, 381. [[CrossRef](#)]
16. Beg, F.N.; Bell, A.R.; Dangor, A.E.; Danson, C.N.; Fews, A.P.; Glinsky, M.E.; Hammel, B.A.; Lee, P.; Norreys, P.A.; Tatarakis, M. A study of picosecond laser-solid interactions up to  $10^{19}$  Wcm<sup>-2</sup>. *Phys. Plasmas* **1997**, *4*, 447. [[CrossRef](#)]
17. Bleko, V.; Karataev, P.; Konkov, A.; Kruchinin, K.; Naumenko, G.; Potylitsyn, A.; Vaughan, T. Coherent Cherenkov radiation as an intense THz source. *J. Phys. Conf. Ser.* **2016**, *732*, 012006. [[CrossRef](#)]
18. Ehret, M.; Cikhardt, J.; Bradford, P.; Vladisavlevici, I.; Burian, T.; de Luis, D.; Henares, J.L.; Martín, R.H.; Apiñaniz, J.I.; Lera, R.; et al. High-repetition-rate source of nanosecond duration kA-current pulses driven by relativistic laser pulses. *High Power Laser Sci. Eng.* **2024**. [[CrossRef](#)]
19. Condamine, F.P.; Jourdain, N.; Hernandez, J.-C.; Taylor, M.; Bohlin, H.; Fajstavr, A.; Jeong, T.M.; Kumar, D.; Laštovička, T.; Renner, O.; et al. High-repetition rate solid target delivery system for PW-class laser-matter interaction at ELI Beamlines. *Rev. Sci. Instruments* **2021**, *90*, 063504. [[CrossRef](#)]
20. Rehwald, M.; Assenbaum, S.; Bernert, C.; Brack, F.E.; Bussmann, M.; Cowan, T.E.; Curry, C.B.; Fiuza, F.; Garten, M.; Gaus, L.; et al. Ultra-short pulse laser acceleration of protons to 80 MeV from cryogenic hydrogen jets tailored to near-critical density. *Nat. Commun.* **2023**, *14*, 4009. [[CrossRef](#)] [[PubMed](#)]
21. Snavely, R.A.; Key, M.H.; Hatchett, S.P.; Cowan, T.E.; Roth, M.; Phillips, T.W.; Stoyer, M.A.; Henry, E.A.; Sangster, T.C.; Singh, M.S.; et al. Intense High-Energy Proton Beams from Petawatt-Laser Irradiation of Solids. *Phys. Rev. Lett.* **2000**, *85*, 2945. [[CrossRef](#)]
22. Wilks, S.C.; Langdon, A.B.; Cowan, T.E.; Roth, M.; Singh, M.; Hatchett, S.; Key, M.H.; Pennington, D.; MacKinnon, A.; Snavely, R.A. Energetic proton generation in ultra-intense laser-solid interactions. *Phys. Plasmas* **2001**, *8*, 542. [[CrossRef](#)]
23. Esirkepov, T.; Borghesi, M.; Bulanov, S.V.; Mourou, G.; Tajima, T. Highly Efficient Relativistic-Ion Generation in the Laser-Piston Regime. *Phys. Rev. Lett.* **2004**, *92*, 175003. [[CrossRef](#)]
24. Nemoto, K.; Maksimchuk, A.; Banerjee, S.; Flippo, K.; Mourou, G.; Umstadter, D.; Bychenkov, V.Y. Laser-triggered ion acceleration and table top isotope production. *Appl. Phys. Lett.* **2001**, *78*, 595–597. [[CrossRef](#)]
25. Ledingham, K.W.D.; McKenna, P.; McCanny, T.; Shimizu, S.; Yang, J.M.; Robson, L.; Zweit, J.; Gillies, J.M.; Bailey, J.; Chimon, G.N.; et al. High power laser production of short-lived isotopes for positron emission tomography. *J. Phys. D Appl. Phys.* **2004**, *37*, 2341. [[CrossRef](#)]
26. Santala, M.I.K.; Zepf, M.; Beg, F.N.; Clark, E.L.; Dangor, A.E.; Krushelnick, K.; Tatarakis, M.; Watts, I.; Ledingham, K.W.D.; McCanny, T.; et al. Production of radioactive nuclides by energetic protons generated from intense laser-plasma interactions. *Appl. Phys. Lett.* **2001**, *78*, 19–21. [[CrossRef](#)]
27. Merrill, F.E.; Golubev, A.A.; Mariam, F.G.; Turtikov, V.I.; Varentsov, D. HEDgeHOB Collaboration Proton Microscopy at FAIR. *AIP Conf. Proc.* **2009**, *1195*, 667–670. [[CrossRef](#)]
28. Mirani, F.; Maffini, A.; Casamichiela, F.; Pazzaglia, A.; Formenti, A.; Dellasega, D.; Russo, V.; Vavassori, D.; Bortot, D.; Huault, M.; et al. Integrated quantitative PIXE analysis and EDX spectroscopy using a laser-driven particle source. *Sci. Adv.* **2021**, *7*, 3. [[CrossRef](#)] [[PubMed](#)]
29. Roth, M.; Cowan, T.E.; Key, M.H.; Hatchett, S.P.; Brown, C.; Fountain, W.; Johnson, J.; Pennington, D.M.; Snavely, R.A.; Wilks, S.C.; et al. Fast Ignition by Intense Laser-Accelerated Proton Beams. *Phys. Rev. Lett.* **2001**, *86*, 436–439. [[CrossRef](#)] [[PubMed](#)]
30. Consoli, F.; Tikhonchuk, V.T.; Bardon, M.; Bradford, P.; Carroll, D.C.; Cikhardt, J.; Cipriani, M.; Clarke, R.J.; Cowan, T.; Danson, C.N.; et al. Laser produced electromagnetic pulses: Generation, detection and mitigation. *High Power Laser Sci. Eng.* **2020**, *8*, e22. [[CrossRef](#)]
31. Brunel, F. Not-so-resonant, resonant absorption. *Phys. Rev. Lett.* **1987**, *59*, 52. [[CrossRef](#)] [[PubMed](#)]
32. Wilks, C.; Kruer, W.L. Absorption of ultrashort, ultra-intense laser light by solids and overdense plasmas. *IEEE J. Quantum Electron.* **1997**, *33*, 1954. [[CrossRef](#)]
33. Wilks, S.C.; Kruer, W.L.; Tabak, M.; Langdon, A.B. Absorption of ultra-intense laser pulses. *Phys. Rev. Lett.* **1992**, *69*, 1383–1386. [[CrossRef](#)]
34. Pukhov, A.; Meyer-ter, V.J. Relativistic laser-plasma interaction by multi-dimensional particle-in-cell simulations. *Phys. Plasmas* **1998**, *5*, 1880–1886. [[CrossRef](#)]
35. Pearlman, J.S.; Dahlbacka, G.H. Charge separation and target voltages in laser-produced plasmas. *Appl. Phys. Lett.* **1977**, *31*, 414–417. [[CrossRef](#)]
36. Courtois, C.; Fontaine, A.C.L.; Landoas, O.; Lidove, G.; Méot, V.; Morel, P.; Nuter, R.; Lefebvre, E.; Boscheron, A.; Grenier, J.; et al. Effect of plasma density scale length on the properties of bremsstrahlung X-ray sources created by picosecond laser pulses. *Phys. Plasmas* **2009**, *16*, 013105. [[CrossRef](#)]
37. Poyé, A.; Hulin, S.; Ribolzi, J.; Bailly-Grandvaux, M.; Lubrano-Lavaderci, F.; Bardon, M.; Raffestin, D.; Santos, J.J.; Tikhonchuk, V. Thin target charging in short laser pulse interactions. *Phys. Rev. E* **2018**, *98*, 033201. [[CrossRef](#)]
38. Rusby, D.R.; Wilson, L.A.; Gray, R.J.; Dance, R.J.; Butler, N.M.H.; MacLellan, D.A.; Scott, G.G.; Bagnoud, V.; Zielbauer, B.; McKenna, P.; et al. Measurement of the angle, temperature and flux of fast electrons emitted from intense laser-solid interactions. *J. Plasma Phys.* **2015**, *81*, 5. [[CrossRef](#)]
39. Dubois, J.-L.; Lubrano-Lavaderci, F.; Raffestin, D.; Ribolzi, J.; Gazave, J.; Fontaine, A.C.L.; d’Humières, E.; Hulin, S.; Nicolai, P.; Poyé, A.; et al. Target charging in short-pulse-laser-plasma experiments. *Phys. Rev. E* **2014**, *89*, 013102. [[CrossRef](#)]

40. Nelissen, K.; Liszi, M.; Marco, M.D.; Ospina, V.; Drotár, I.; Gatti, G.; Kamperidis, C.; Volpe, L. Characterisation and Modelling of Ultrashort Laser-Driven Electromagnetic Pulses. *Sci. Rep.* **2020**, *10*, 3108. [[CrossRef](#)]
41. Shurenkov, V.V.; Pershenkov, V.S. Electromagnetic effects and damage mechanism on the semiconductor electronics. *Facta Univ. Ser. Electron. Energetics* **2016**, *29*, 621–629. [[CrossRef](#)]
42. Volpe, L.; Fedosejevs, R.; Gatti, G.; Pérez-Hernández, J.A.; Méndez, C.; Apiñaniz, J.; Vaisseau, X.; Salgado, C.; Huault, M.; Malko, S.; et al. Generation of high energy laser-driven electron and proton sources with the 200 TW system VEGA 2 at the Centro de Laseres Pulsados. *High Power Laser Sci. Eng.* **2019**, *7*, e25. [[CrossRef](#)]
43. Kluge, T.; Cowan, T.; Debus, A.; Schramm, U.; Zeil, K.; Bussmann, M. Electron Temperature Scaling in Laser Interaction with Solids. *Phys. Rev. Lett.* **2011**, *107*, 205003. [[CrossRef](#)]
44. Roth, M.; Schollmeier, M. Ion Acceleration—Target Normal Sheath Acceleration. In Proceedings of the 2014 CAS-CERN Accelerator School: Plasma Wake Acceleration, Geneva, Switzerland, 23–29 November 2014. [[CrossRef](#)]
45. Vertes, A.; Wolf, M.D.; Juhasz, P.; Gijbels, R. Threshold conditions of plasma ignition in laser ionization mass spectrometry of solids. *Anal. Chem.* **1989**, *61*, 1029–1035. [[CrossRef](#)]
46. Drouin, D.; Couture, A.R.; Joly, D.; Tastet, X.; Aimez, V.; Gauvin, R. CASINO V2.42—A Fast and Easy-to-use Modeling Tool for Scanning Electron Microscopy and Microanalysis Users. *Scanning* **2007**, *29*, 92–101. [[CrossRef](#)] [[PubMed](#)]
47. Lancaster, K.L.; Karsch, S.; Habara, H.; Beg, F.N.; Clark, E.L.; Freeman, R.; Key, M.H.; King, J.A.; Kodama, R.; Krushelnick, K.; et al. Characterization of neutron yields from laser produced ion beams for fast neutron radiography. *Phys. Plasmas* **2004**, *11*, 3404–3408. [[CrossRef](#)]
48. Higginson, D.P.; McNaney, J.M.; Swift, D.C.; Petrov, G.M.; Davis, J.; Frenje, J.A.; Jarrott, L.C.; Kodama, R.; Lancaster, K.L.; Mackinnon, A.J.; et al. Production of neutrons up to 18 MeV in high-intensity short-pulse laser matter interactions. *Phys. Plasmas* **2011**, *18*, 100703. [[CrossRef](#)]
49. Deng, H.X.; Sha, R.; Hu, L.X.; Jiang, X.R.; Zhao, N.; Zou, D.B.; Yu, T.P.; Shao, F.Q. Pulsed neutron source from interaction of relativistic laser pulse with micro-structure assisted pitcher-catcher target. *Plasma Phys. Control. Fusion* **2022**, *64*, 085004. [[CrossRef](#)]
50. Jiang, X.R.; Shao, F.Q.; Zou, D.B.; Yu, M.Y.; Hu, L.X.; Guo, X.Y.; Huang, T.W.; Zhang, H.; Wu, S.Z.; Zhang, G.B.; et al. Energetic deuterium-ion beams and neutron source driven by multiple-laser interaction with pitcher-catcher target. *Nucl. Fusion* **2020**, *60*, 076019. [[CrossRef](#)]
51. Baker, G.H. Electromagnetic Pulse Resilience of United States Critical Infrastructure: Progress and Prognostics. *J. Crit. Infrastruct. Policy* **2021**, *2*, 1. [[CrossRef](#)]
52. Kim, J.H.; Lee, J.; Kim, H.; Kim, K.; Kim, H.R. Possible Effects of Radiofrequency Electromagnetic Field Exposure on Central Nerve System. *Biomol. Ther.* **2019**, *27*, 265–275. [[CrossRef](#)]

**Disclaimer/Publisher’s Note:** The statements, opinions and data contained in all publications are solely those of the individual author(s) and contributor(s) and not of MDPI and/or the editor(s). MDPI and/or the editor(s) disclaim responsibility for any injury to people or property resulting from any ideas, methods, instructions or products referred to in the content.